

Accepted for publication in the Astrophysical Journal

**On the Expansion Rate, Age, and Distance of the Supernova Remnant  
G266.2–1.2 (Vela Jr.)**

G. E. Allen

*MIT Kavli Institute for Astrophysics and Space Research, 77 Massachusetts Avenue, NE83-557,  
Cambridge, MA 02139*

`gea@space.mit.edu`

K. Chow

*Weston High School, 444 Wellesley Street, Weston, MA 02493*

`kc71135@gmail.com`

T. DeLaney

*Department of Physics and Engineering, West Virginia Wesleyan College, Box 112, 59 College  
Avenue, Buckhannon, WV 26201*

`delaney_t@wvwc.edu`

M. D. Filipović

*University of Western Sydney, Locked Bag 1797, Penrith South DC, NSW 1797, Australia*

`m.filipovic@uws.edu.au`

J. C. Houck

*MIT Kavli Institute for Astrophysics and Space Research, 77 Massachusetts Avenue, NE80-6023,  
Cambridge, MA 02139*

`houck@space.mit.edu`

T. G. Pannuti

*Space Science Center, Department of Earth and Space Sciences, Morehead State University, 235  
Martindale Drive, Morehead, KY 40351*

`t.pannuti@moreheadstate.edu`

and

M. D. Stage

*University of Massachusetts, Department of Astronomy, LGRT-B 619E, 710 North Pleasant Street, Amherst, MA 01003-9305*

mikstage@astro.umass.edu

## ABSTRACT

An analysis of *Chandra* ACIS data for two relatively bright and narrow portions of the northwestern rim of G266.2–1.2 (a.k.a. RX J0852.0-4622 or Vela Jr.) reveal evidence of a radial displacement of  $2.40 \pm 0.56$  arcsec between 2003 and 2008. The corresponding expansion rate ( $0.42 \pm 0.10$  arcsec yr<sup>-1</sup> or  $13.6 \pm 4.2\%$  kyr<sup>-1</sup>) is about half the rate reported for an analysis of *XMM-Newton* data from a similar, but not identical, portion of the rim over a similar, but not identical, time interval ( $0.84 \pm 0.23$  arcsec yr<sup>-1</sup>, Katsuda et al. 2008a). If the *Chandra* rate is representative of the remnant as a whole, then the results of a hydrodynamic analysis suggest that G266.2–1.2 is between 2.4 and 5.1 kyr old if it is expanding into a uniform ambient medium (whether or not it was produced by a Type Ia or Type II event). If the remnant is expanding into the material shed by a steady stellar wind, then the age could be as much as 50% higher. The *Chandra* expansion rate and a requirement that the shock speed be greater than or equal to 1000 km s<sup>-1</sup> yields a lower limit on the distance of 0.5 kpc. An analysis of previously-published distance estimates and constraints suggests G266.2–1.2 is no further than 1.0 kpc. This range of distances is consistent with the distance to the nearer of two groups of material in the Vela Molecular Ridge ( $0.7 \pm 0.2$  kpc, Liseau et al. 1992) and to the Vel OB1 association (0.8 kpc, Eggen 1982).

*Subject headings:* ISM: individual objects (G266.2–1.2) — ISM: supernova remnants — shock waves — X-rays: individual (G266.2–1.2)

## 1. Introduction

The shell-type supernova remnant G266.2–1.2 was discovered in the *ROSAT* all-sky survey data and, based upon its equatorial coordinates, named RX J0852.0–4622 (Aschenbach 1998). It lies along the same line of sight as the Vela supernova remnant, which is considerably brighter than G266.2–1.2 (Vela-Z) at radio frequencies (Milne 1968; Bock et al. 1998; Combi et al. 1999) and at X-ray energies below 1 keV (Aschenbach 1998). For these reasons, it is not surprising that G266.2–1.2 (aka “Vela Jr.”) was only recently identified as a separate object.<sup>1</sup>

---

<sup>1</sup>Wang & Chevalier (2002) consider the possibility that G266.2–1.2 may not be a separate object, but is instead part of the Vela supernova remnant, produced by a fast-moving ejecta clump that has interacted with the shell. Here,

The remnant is nearly circular with a relatively large angular radius of about  $0.9^\circ$ . It has relatively low radio (Duncan & Green 2000) and X-ray surface brightnesses. To the extent that it is possible to distinguish the emission of G266.2–1.2 from the emission of Vela, the X-ray (Slane et al. 2001; Bamba et al. 2005; Pannuti et al. 2010) and radio spectra of G266.2–1.2 appear to be dominated by synchrotron radiation (or, perhaps, jitter radiation, Ogasawara et al. 2007) from TeV and GeV electrons, respectively. Images in these two wavelengths are fairly similar to one another (Stupar et al. 2005) and to a TeV gamma-ray image (Aharonian et al. 2007). The detection of TeV gamma rays (Katagiri et al. 2005; Aharonian et al. 2005; Enomoto et al. 2006; Aharonian et al. 2007) provides unequivocal evidence of the presence of TeV cosmic rays. Tanaka et al. (2011) and Lande et al. (2012) report the detection of G266.2–1.2 in GeV gamma rays. However, images at this energy differ somewhat from the TeV gamma-ray, X-ray, and radio images, perhaps due to a spatially unresolved (at GeV energies) combination of emission from G266.2–1.2 and from the pulsar wind nebula of PSR J0855–4644.

The 64.7 ms radio pulsar PSR J0855–4644 (Kramer et al. 2003), which lies near the southeastern rim of G266.2–1.2, is associated with an X-ray-emitting (Acero et al. 2013) and, perhaps, gamma-ray-emitting (Aharonian et al. 2007; Tanaka et al. 2011; Lande et al. 2012) pulsar wind nebula. However, Acero et al. (2013) argue that the idea that PSR J0855–4644 and G266.2–1.2 are associated with each other (Redman & Meaburn 2005) is unlikely because the space velocity of the pulsar would have to be unusually high and because there is no evidence of a bow shock or a trail around it. Furthermore its characteristic age (140 kyr, Kramer et al. 2003) exceeds our age range for G266.2–1.2 (2.4–5.1 kyr) by more than an order of magnitude.

There is a compact X-ray-emitting object (CXOU J085201.4–461753) near the geometric center of G266.2–1.2 (Aschenbach 1998; Slane et al. 2001; Mereghetti 2001; Pavlov et al. 2001; Kargaltsev et al. 2002) at least in the plane of the sky. This compact object and the supernova remnant may also lie at the same distance since (model-dependent) estimates of the absorption column density to the object ( $n_{\text{H}} \sim 0.3\text{--}1.1 \times 10^{22} \text{ cm}^{-2}$ , Pavlov et al. 2001; Kargaltsev et al. 2002; Becker et al. 2006) are similar to estimates of the absorption column density to the remnant ( $n_{\text{H}} \sim 0.1\text{--}1.1 \times 10^{22} \text{ cm}^{-2}$ , Aschenbach 1998; Tsunemi et al. 2000; Slane et al. 2001; Iyudin et al. 2005; Bamba et al. 2005; Acero et al. 2013).<sup>2</sup> The lack of evidence of R band emission from CXOU J085201.4–461753, down to a limiting magnitude of about 25.6 (Mignani et al. 2007), suggests that it was produced by the collapse of a massive star (Pavlov et al. 2001). There is no

---

we assume that G266.2–1.2 and Vela are separate objects because the spectral properties of G266.2–1.2 and the Vela ejecta clumps “A” and “D” are not the same. Features “A” (Miyata et al. 2001; Katsuda & Tsunemi 2006) and “D” (Plucinsky et al. 2002; Katsuda & Tsunemi 2005) exhibit thermal X-ray spectra, while X-ray spectra of G266.2–1.2 seem to be entirely nonthermal. Furthermore, G266.2–1.2 is a source of TeV gamma rays, and at least feature “D” is not (Aharonian et al. 2007, Figs. 1, 3, 4).

<sup>2</sup>While the association of CXOU J085201.4–461753 and G266.2–1.2 seems plausible, we cannot exclude the possibility that they are unrelated because the estimates of the absorption column densities are uncertain and because this region of the sky is fairly busy.

evidence of X-ray pulsations (Becker et al. 2006) or of a known radio pulsar at this location.<sup>3</sup> The object does lie in or near a 6 arcsec-diameter optically-emitting nebula (Pellizzoni et al. 2002; Mignani et al. 2007), at least on the plane of the sky, but it is not clear that the detected optical (H $\alpha$  or [NII]) source and the X-ray source are the same object (Mignani et al. 2009).

The complexity of the region makes it difficult to make a strong statement, but G266.2–1.2 does not appear to be a source of neutral hydrogen (Dubner et al. 1998; Testori et al. 2006), infrared (Nichols & Slavin 2004), [OIII] (Filipović et al. 2001), or far-ultraviolet (Nishikida et al. 2006; Kim et al. 2012) emission.

We used the *Chandra* telescope to observe the thin filaments in the bright northwestern region of G266.2–1.2 on two separate occasions. These data and the techniques used to analyze them are described in §2. Constraints on the age and distance of the remnant are discussed in §3. The conclusions are presented in §4.

## 2. Data and Analyses

The northwestern region of G266.2–1.2 was observed with *Chandra*<sup>4</sup> in 2003 (Bamba et al. 2005; Pannuti et al. 2010) and 2008 (Table 1). The data for these observations were reprocessed with version 4.6 of the CIAO suite of analysis tools<sup>5</sup> and with version 4.6.1.1 of the CALDB<sup>6</sup> to use the most recent data reduction algorithms and calibration products. This process involved the following steps, in sequence. The Level 1 event-data status bits 1–5 and 14–23 (of 0–31) were unset. The tool `destreak` was used to identify events associated with horizontal streaks (electronic noise) on the ACIS-S4 CCD. The tools `acis_build_badpix` (first execution), `acis_find_afterglow`, and `acis_build_badpix` (second execution) were used to produce new observation-specific bad-pixel files. Note that the tool `acis_find_afterglow` includes the most recent cosmic-ray afterglow and hot-pixel identification algorithms. The tool `acis_process_events` was used to apply the new bad-pixel files, to update the computation of the celestial coordinates, to update the pulse-height information (i.e. the charge-transfer inefficiency (CTI) and time-dependent gain adjustments), and to set certain status bits. The tool `dmcopy` was used to exclude events that are not in the good-time intervals, that have a bad grade (1, 5, or 7), that have one or more status bits set to one (e.g. occur on bad pixels or that are part of an afterglow or horizontal ACIS-S4 streak), or that have an energy outside the range from 1–5 keV. The data at energies less than 1 keV were discarded because they are dominated by emission from the foreground Vela supernova remnant (Aschenbach 1998). The

---

<sup>3</sup>See the ATNF Pulsar Catalogue at <http://www.atnf.csiro.au/people/pulsar/psrcat/> (Manchester et al. 2005).

<sup>4</sup>The *Chandra X-ray Observatory* is described in the *Chandra* Proposers’ Observatory Guide, which is available at <http://cxc.harvard.edu/proposer/POG/>.

<sup>5</sup>More information about CIAO is available at <http://cxc.harvard.edu/ciao/>.

<sup>6</sup>More information about the CALDB is available at <http://cxc.harvard.edu/caldb/>.

data at energies greater than or equal to 5 keV were discarded because they are dominated by a charged-particle background. There is no evidence of significant problems with the bias maps or of flares in the particle background. The focal-plane temperature remained within 1 °C of the nominal temperature of  $-119.7$  °C.

Figures 1 and 2 are images of the 1–5 keV photon fluxes incident on the *Chandra* telescope (i.e. the absorbed fluxes) in 2003 and 2008, respectively. These images were produced using the following CIAO tools in sequence: `reproject_events` (to place the data for OBS\_IDs 4414 and 9123 on the same celestial tangent plane as the data for OBS\_ID 3846), `asphist`, `mkinstmap` (with spectral weights from the spectrum of the brightest portion of the region that was observed in both epochs),<sup>7</sup> `mkexppmap`, `dmcopy`, and `dmimgcalc`. The point-spread function of the *Chandra* mirrors and ACIS varies over the observed portion of G266.2–1.2. At the aim point, 50% of the events fall within a radius of about  $0.5''$ . For a region that is  $10'$  off axis, this radius is about  $5''$ . Version 6.11 of the FTOOL<sup>8</sup> `fgauss` was used to smooth the images with a two-dimensional Gaussian function where  $\sigma_X = \sigma_Y = 10$  pixels = 4.92 arcsec. This choice of Gaussian widths yields images that have comparable spatial resolutions in the regions that were used to measure the rate of expansion. While the procedure used to create Figures 1 and 2 removed most of the instrumental features, some residual artifacts remain, particularly between CCDs and along the outer edges of the detectors.

The images were searched for potential registration sources. The two sources listed in Table 2 and shown in Figures 1 and 2, while faint, are point-like, are present in both the 2003 and 2008 datasets, seem to be spatially coincident with sources in the *2MASS*<sup>9</sup> and USNO-B1.0<sup>10</sup> catalogs, and, at least for the 2003 observation, are moderately close to the optical axis of *Chandra*. These criteria give us some confidence that the sources are not associated with diffuse emission from the remnant. The *Chandra* coordinates listed in Table 2 were computed for each source at each epoch as follows. A bin size in the range from 0.3 to 2.0 pixels (i.e. 0.15 to 0.98 arcsec) was chosen. The events located within a  $60$  bin  $\times$   $60$  bin square grid centered on the *2MASS* coordinates of the source were selected. A one-dimensional, 60-bin histogram of these events was created along the  $X$  axis (i.e. Right Ascension) and fitted with a model that includes a constant component for the background and a Gaussian component for the source. The four parameters for this model were allowed to vary. A similar histogram was created along the  $Y$  axis (i.e. Declination) and a similar fit was performed. This process was repeated for many bin sizes. While the results at all bin sizes are consistent with the results in Table 2, in general the results seem most reliable for bin sizes between about 0.5 and 1.0 pixels. Therefore, the coordinates in this Table are the mean values of the results obtained for bin sizes in this narrower range. The *Chandra* and USNO-B1.0 coordinates are plotted relative to the *2MASS* coordinates in the four panels of Figure 3. Since

---

<sup>7</sup>Spatial variations in the shape of the spectrum can lead to systematic errors in the relative flux.

<sup>8</sup>More information about FTOOLS is available at [http://heasarc.nasa.gov/ftools/ftools\\_menu.html](http://heasarc.nasa.gov/ftools/ftools_menu.html).

<sup>9</sup>The *2MASS* All-Sky Point Source Catalog is available at <http://www.ipac.caltech.edu/2mass/releases/allsky/>.

<sup>10</sup>The USNO-B1.0 catalog (Monet et al. 2003) is available at <http://www.usno.navy.mil/USNO/astrometry/optical-IR-prod/usno-b1>.

the 2MASS coordinates are used for reference here, they are plotted at the centers of the four panels. The lengths of the horizontal and vertical bars for each data point correspond to the 90% confidence level intervals in Right Ascension and Declination, respectively. The value of  $\Psi$  in each panel of the Figure denotes the angle between the optical axis of the *Chandra* telescope and the 2MASS coordinates of the source. The wide range of these angles (0.90 to 6.15 arcmin), suggests that the *Chandra* coordinates are affected to varying degrees by asymmetries in the off-axis point-spread function of the telescope. MARX<sup>11</sup> simulations were used to investigate this effect. About  $10^7$  simulated X-rays were produced for each source at each epoch assuming that the sources are at the locations given by the 2MASS coordinates. A subset of the simulated events were used to calculate the coordinates in the manner described above. The number of events in each subset is consistent with the number of events in the *Chandra* data. Ten thousand subsets were processed for each one of the four cases (i.e. each one of the four panels in Fig. 3). The horizontal and vertical bars of the blue data points in Figure 3 represent the intervals over which 90% of the simulated Right Ascension and Declination coordinates, respectively, are found. As shown, the simulated locations of the 2MASS sources are consistent with the actual 2MASS locations. Therefore, asymmetries in the off-axis point-spread function of the *Chandra* telescope are not expected to significantly affect the accuracy of the *Chandra* coordinates of the registration sources. From Table 2, the differences between the *Chandra* coordinates of the registration sources in 2003 and the 2MASS coordinates of the sources are  $\Delta\alpha \equiv \alpha_{Chandra} - \alpha_{2MASS} = -0.04 \pm 0.08$  arcsec and  $\Delta\delta \equiv \delta_{Chandra} - \delta_{2MASS} = 0.11 \pm 0.08$  arcsec. In 2008, the differences are  $\Delta\alpha = -0.33 \pm 0.18$  arcsec and  $\Delta\delta = -0.25 \pm 0.31$  arcsec. With the possible exception of source 1 in 2008, (i.e. the upper, right-hand panel in Figure 3), there is no compelling evidence that the locations of the sources in the *Chandra* data are inconsistent with the locations of the 2MASS sources. For this reason, the images shown in Figures 1 and 2 have not been adjusted to compensate for any potential registration errors.

After determining that the 2003 and 2008 datasets are registered to an accuracy of about 0.5 arcsec (1 pixel) or better, the rate of expansion was measured in annular wedges A and B (Figures 1 and 2) as follows. For each epoch, an image was created in the sky coordinates  $X$  and  $Y$ . These images have 1 pixel  $\times$  1 pixel (i.e. 0.492 arcsec  $\times$  0.492 arcsec) bins and were smoothed with a two-dimensional Gaussian function where  $\sigma_X = \sigma_Y = 10$  pixels = 4.92 arcsec.<sup>12</sup> This choice of Gaussian widths yields 2003 and 2008 images that have comparable spatial resolutions in regions A and B. The two sky images were used to create images in the coordinates  $\theta$  and  $\phi$ . Here,  $\theta$  is the angular radius (or angular separation) of a point in the *Chandra* data from the assumed location

---

<sup>11</sup>More information about the MARX simulator is available at <http://space.mit.edu/cxc/marx/>.

<sup>12</sup>Several values for the Gaussian width  $\sigma = \sigma_X = \sigma_Y$  were tried from 5 to 20 pixels. While there is some indication that the measured values of the radial offset  $\Delta\theta$  decline with increasing smoothing size  $\sigma$ , the best-fit values seem to be insensitive to the smoothing size for  $\sigma \leq 10$  pixels. Note that in no case were the best-fit values inconsistent with the values listed in Table 3. In fact, the fitted parameters were well within the 90% confidence intervals even at  $\sigma = 20$  pixels.

of the center of the remnant. Since the location at which the progenitor exploded is unknown, the center is assumed to be the location of the source CXOU J085201.4–461753 ( $\alpha_{\text{J2000}} = 8^{\text{h}} 52^{\text{m}} 01^{\text{s}}.38$  and  $\delta_{\text{J2000}} = -46^{\circ} 17' 53''.34$ , Pavlov et al. 2001), which may be a compact object associated with G266.2–1.2. For calculations that depend upon the value of  $\theta$ , a 20% uncertainty is assumed because the remarkable correlation between the outer edge of the shock and a circular arc with CXOU J085201.4–461753 as the focus (Figs. 1 and 2) becomes rather poor if the location the focus (and the corresponding angular radius) is shifted by 20% or more of the angular radius. The angle  $\phi$  is the azimuth. It is measured from north ( $\phi = 0^{\circ}$ ) through east ( $\phi = 90^{\circ}$ ) relative to the center of the remnant. The images in  $\theta$  and  $\phi$  also have  $0.492 \text{ arcsec} \times 0.492 \text{ arcsec}$  bins. Radial profiles were obtained from the  $\theta$  and  $\phi$  images by summing along the  $\phi$  direction. The radial offset of the 2008 data with respect to the 2003 data was obtained by interpolating each radial profile to a grid with a spacing of  $10^{-4}$  pixels (i.e.  $4.92 \times 10^{-5}$  arcsec) and by minimizing the fit statistic

$$\chi^2 = \sum_{i=1}^n \left( \frac{C_{2008,i} - M_i}{\sigma_i} \right)^2, \quad (1)$$

where the “model”

$$M_i = s (C_{2003,i-j} - \Sigma_{B,2003}\Omega_{i-j}) + \Sigma_{B,2008}\Omega_i, \quad (2)$$

where the statistical uncertainty

$$\sigma_i = (C_{2008,i} + s^2 C_{2003,i-j})^{1/2}, \quad (3)$$

and where  $C_{2003,i}$  and  $C_{2008,i}$  are the total number of events in the  $i$ th bin of the interpolated radial profiles for the 2003 and 2008 data, respectively,  $\Sigma_{B,2003}$  and  $\Sigma_{B,2008}$  are the number of background events per square arcsec for the 2003 and 2008 data, respectively,  $\Omega_i$  is the number of square arcseconds in the  $i$ th bin,  $s$  is a scaling factor, which compensates for differences in the detector efficiencies, observing times, and source fluxes in the two epochs, and  $j$  is the radial offset of the 2008 data relative to the 2003 data in units of  $10^{-4}$  pixels. In equation 3, the statistical uncertainty includes contributions for both datasets. During the fitting process, the value of  $\chi^2$  was calculated using many sets of values for the two variables  $s$  and  $j$ , both of which were allowed to vary freely. The values of  $\Sigma_{B,2003}$  and  $\Sigma_{B,2008}$  were frozen at the values listed in Table 3.<sup>13</sup> These values were obtained from the numbers of events in and the sizes of the source free portions of the two regions. The best-fit results for regions A and B are listed in Table 3. This Table includes the parameter  $\Delta\theta = 4.92 \times 10^{-5}j$ . Since  $j$  is quantized in units of  $10^{-4}$  pixels,  $\Delta\theta$  is in units of arcsec. The uncertainties are listed at the 90% confidence level, which corresponds to a change in  $\chi^2$  of 2.71. Both of the parameters  $s$  and  $j$  were allowed to vary while the confidence intervals were being computed. Figure 4 shows profiles of  $C_{2008}$ ,  $M$  (with  $\Delta\theta = 0$  arcsec), and  $M$  (with

---

<sup>13</sup>Some fits were performed with the values of  $\Sigma_{B,2003}$  and  $\Sigma_{B,2008}$  allowed to vary freely. In these cases, the best-fit values for these two parameters and for  $s$  and  $j$  were consistent with the values listed in Table 3. Since the value of  $\chi^2$  seems to be rather insensitive to the values of  $\Sigma_{B,2003}$  and  $\Sigma_{B,2008}$  and since there was some difficulty obtaining meaningful confidence level uncertainties for these two parameters, their values were frozen in all other fits.

$\Delta\theta = 2.0$  arcsec) for region A. Figure 5 shows the 1-, 2-, and 3- $\sigma$  confidence contours (i.e. where  $\chi^2$  changes by 2.30, 6.18, and 11.83) in the parameter space defined by  $\Delta\theta$  and  $s$  for the same region.

There is significant evidence that the shock front of G266.2–1.2 expanded from 2003 to 2008, at least in regions A and B. The amounts of expansion for these two regions are consistent with one another at the 90% confidence level (Table 3) and are insensitive to the mean registration adjustments (e.g. Figure 5). Since there is no compelling evidence that the registration of the *Chandra* data is inaccurate, the results presented hereafter are the results obtained without registration adjustments and the uncertainties are quoted at the 90% confidence level. The mean amount of expansion for regions A and B is  $\Delta\theta = 2.40 \pm 0.56$  arcsec over a period of 5.652 yr, which corresponds to an expansion rate of  $\dot{\theta} = 0.42 \pm 0.10$  arcsec yr<sup>-1</sup>. If the shock radius  $\theta = 0.86^\circ$ , the angular distance between CXOU J085201.4–461753 and the northwestern rim (Fig. 4), then the fractional expansion rate  $\dot{\theta}/\theta = 0.136 \pm 0.042$  kyr<sup>-1</sup>.

If the flux from regions A and B of G266.2–1.2 did not change, then the scaling factors  $s$  should be consistent with the ratios  $\Sigma_{B,2008}/\Sigma_{B,2003}$  of the background event densities. These ratios are  $0.331 \pm 0.048$  and  $0.332 \pm 0.049$ , respectively, for regions A and B, which are consistent with the best-fit values of  $s$ . Therefore, there is no evidence of significant flux changes from 2003 to 2008 for these two regions.

### 3. Discussion

#### 3.1. Age

The expansion rate measured using *Chandra* data ( $0.42 \pm 0.10$  arcsec yr<sup>-1</sup>) is about half the expansion rate obtained using *XMM-Newton* data ( $0.84 \pm 0.23$  arcsec yr<sup>-1</sup>, Katsuda et al. 2008a). The two measurements are from similar time intervals (2003 to 2008 for *Chandra* and 2001 to 2007 for *XMM-Newton*) and from similar regions (i.e. bright portions of the northwestern rim). However, the regions used are not identically the same. It is possible that there is an azimuthal variation in the expansion rate along the northwestern rim of G266.2–1.2. Although the difference is not statistically significant, the expansion rates in regions A and B differ by a factor of 1.5 (Table 3). While there may not be significant differences in the expansion rates along the northeastern rim of SN 1006 (Katsuda et al. 2009), there do appear to be significant azimuthal variations in the expansion rates of Cas A (DeLaney & Rudnick 2003) and Kepler (Katsuda et al. 2008b). Furthermore, the variations reported for these latter two remnants could be as large as a factor of two or more.

If the angular radius  $\theta = 0.86^\circ$ , then the fractional expansion rates  $\dot{\theta}/\theta$  are  $0.136 \pm 0.042$  kyr<sup>-1</sup> and  $0.27 \pm 0.07$  kyr<sup>-1</sup> for *Chandra* and *XMM-Newton*, respectively.<sup>14</sup> The fractional expansion

---

<sup>14</sup>Katsuda et al. (2008a) assume an angular radius of  $1^\circ$  instead of  $0.86^\circ$ . Therefore, they report a fractional



rate provides a crude constraint on the age of the remnant. If the radius of the forward shock  $r_f \propto t^m$ , where  $t$  is the age and  $m$  is the expansion parameter, and if  $m$  is a constant over the time interval of the expansion measurement, then  $t = m\theta/\dot{\theta}$ . While the value of  $m$  is unknown, it is most likely in the range from 0.4 (the Sedov-Taylor phase) to 1 (the free-expansion phase). In this case, the age of G266.2–1.2 is in the range<sup>15</sup> from 2.1 to 13 kyr (*Chandra*) or from 1.2 to 5.0 kyr (*XMM-Newton*), provided the expansion results for the northwestern rim are representative of the remnant as a whole.

To try to obtain better constraints on the age of G266.2–1.2, we used the hydrodynamic models of Truelove & McKee (1999). Since the physical conditions—the initial kinetic energy ( $E_0$ ), mass ( $M_{\text{ej}}$ ), and mass density distribution ( $\rho_{\text{ej}} \propto v^{-n}t^{-3}$ ) of the ejecta, the ambient mass density distribution ( $\rho_0 = 1.42m_p n_0$ ), and the evolutionary state ( $t/t_{\text{ch}}$ )—are unknown, a five-dimensional grid in  $E_0$ ,  $M_{\text{ej}}$ ,  $n$ ,  $n_0$ , and  $t/t_{\text{ch}}$  was used with 81 values of  $E_0$ :  $10^{49}$ ,  $10^{49.05}$ ,  $\dots$ ,  $10^{53}$  ergs; 41 values of  $M_{\text{ej}}$ :  $10^0$ ,  $10^{0.05}$ ,  $\dots$ ,  $10^2 M_{\odot}$ ; seven values of  $n$ : 6, 7, 8, 9, 10, 12, 14 (i.e.  $m = (n-3)/n = 0.50, \dots, 0.79$ ); 101 values of  $n_0$ :  $10^{-5}$ ,  $10^{-4.95}$ ,  $\dots$ ,  $10^0 \text{ cm}^{-3}$ ; and 999 values of  $t/t_{\text{ch}}$ : 0.01, 0.02,  $\dots$ , 9.99. Note that the characteristic age  $t_{\text{ch}} = 6.18 (E_0/10^{51} \text{ ergs})^{-1/2} (M_{\text{ej}}/10M_{\odot})^{5/6} (n_0/0.1 \text{ cm}^{-3})^{-1/3}$  kyr. Collectively, the grid includes 2.35 billion scenarios. Of course, most of the scenarios are improbable. We tried to make the range of values for each parameter large enough to bracket the expected value of the parameter. The following four criteria were used to determine which scenarios and, hence, which ages, are plausible.

One criteria is that the distance-independent fractional expansion rate (i.e.  $v_f/r_f = \dot{\theta}/\theta$ ) must be compatible with the *Chandra* result (i.e. is in the range from 0.094 to  $0.178 \text{ kyr}^{-1}$ ). Scenarios that did not satisfy this criteria were discarded.

Another criteria is that the forward shock speed must be greater than or equal to  $1000 \text{ km s}^{-1}$ . Such speeds are required (e.g. eqn. A5 of Allen et al. 2008) to accelerate electrons to energies high enough to produce X-ray synchrotron spectra with cut-off frequencies in excess of  $10^{17} \text{ Hz}$  (Pannuti et al. 2010).

A third criteria is that the inferred amount of thermal X-ray emission from the forward-shocked material cannot exceed observational constraints. The pshock model of XSPEC was used to describe this emission. The abundances were assumed to be solar and the temperature was set to 0.3 keV. While the temperature is unknown, it is expected to be at least this high since the electron temperatures measured for other X-ray synchrotron-emitting remnants are larger. Had a higher temperature been used, then more scenarios would have been discarded. The lower and upper limits on the pshock ionization timescale were set to zero and  $1.2n_0t$ , respectively. The pshock normalization was set to  $3.64 \times 10^{-18} (n_0/1 \text{ cm}^{-3})^2 (r_f/1 \text{ cm}) \text{ cm}^{-5}$ . This value is based upon the assumptions that the shock-heated gas fills one quarter of the volume inside the forward

---

expansion rate of  $0.23 \pm 0.06 \text{ kyr}^{-1}$  instead of the rate of  $0.27 \pm 0.07 \text{ kyr}^{-1}$  that we use for comparison.

<sup>15</sup>These ranges include the 90% confidence level uncertainty on  $\dot{\theta}/\theta$ .

shock and that it has an electron-to-proton ratio of 1.2 (i.e. that the proton and electron densities are  $4n_0$  and  $4.8n_0$ , respectively). The pshock emission is absorbed using the XSPEC model `tbabs` with  $n_{\text{H}} = 1.2 \times 10^{22}$  atoms  $\text{cm}^{-2}$ . This absorption column density represents an upper limit for the remnant (Acero et al. 2013). Lower column densities would have resulted in more scenarios being discarded. The absorbed thermal X-ray spectrum was compared to the total *ROSAT* spectrum for a  $0.86^\circ$  radius cone along the line of sight through G266.2–1.2. This spectrum includes emission from both the G266.2–1.2 and Vela supernova remnants. As long as the absorbed emission model for a scenario does not exceed the *ROSAT* spectrum by more than  $3\sigma$  at any point in the spectrum, the scenario is considered plausible. This constraint limits the ambient density to be below  $0.4 \text{ cm}^{-3}$ .

The last criteria used is an energy constraint. The sum of the kinetic and thermal energies of the forward-shocked material plus the inferred energy of the cosmic-ray protons cannot exceed  $E_0$ , the initial kinetic energy of the ejecta. This constraint is less restrictive than it would have been if the computation also included the energies associated with the shocked and unshocked ejecta, with the other cosmic-ray particles, and with the magnetic field. The kinetic energy of the forward-shocked material is assumed to be given by  $U_{\text{KE},f} = 3\pi\rho_0 r_f^3 v_f^2 / 8$  (i.e.  $= M_s (3v_f/4)^2 / 2$ , where  $M_s = 4\pi\rho_0 r_f^3 / 3$ ). The thermal energy of the forward-shocked material is assumed to be given by the same expression (i.e.  $U_{kT,f} = \sum_i 3N_i kT_i / 2$ , where  $N_i = 4\pi\rho_i r_f^3 / (3m_i)$  and  $kT_i = 3m_i v_f^2 / 16$ ). The total energy in cosmic-ray protons is obtained by integrating the momentum-dependent energy over the power-law number-density distribution  $dn/dp = A(p/p_0)^{-\Gamma} \exp(-(p-p)/p_{\text{max}})$  and by multiplying by one quarter of the total volume. Here,  $A = 3.5 \times 10^{-8} \text{ cm}^{-3} (\text{GeV}/c)^{-1}$ ,  $p_0 = 1 \text{ GeV}/c$ ,  $\Gamma = 2.0$ , and  $p_{\text{max}} = 18 \text{ TeV}/c$ . These parameters are based on a joint fit of an inverse Compton model to gamma-ray data and of a synchrotron model to radio and X-ray data (see Allen et al. 2011). The number density of protons is assumed to be one hundred times larger than the number density of electrons at  $p = 1 \text{ GeV}/c$ . A larger proton-to-electron ratio would have lead to more scenarios being discarded. The integration is performed from  $p_{\text{min}}$  to  $10p_{\text{max}}$ . The former quantity is the momentum at which there is a transition from a Maxwell-Boltzmann distribution to the power-law. Implicit in this calculation is the requirement that the number density of thermal protons must exceed the number density of nonthermal protons at thermal momenta. The energy constraint limits  $E_0$  to be above  $4 \times 10^{49}$  ergs,  $n_0$  to be above  $3 \times 10^{-4} \text{ cm}^{-3}$ ,  $r_f$  to be less than 70 pc (i.e.  $d < 5 \text{ kpc}$ ), and  $v_f$  to be less than  $10^4 \text{ km s}^{-1}$ .

Of the 2.35 billion scenarios considered, 57.4 million (2.45%) satisfy all four of our plausibility criteria. A histogram of the ages for the plausible scenarios is shown in Figure 6. The youngest plausible scenario has an age of 2.2 kyr. The oldest is 8.4 kyr. If the lowest 5% and highest 5% of the distribution are discarded, then the 90% confidence level interval for the age is from 2.4 to 5.1 kyr.

This range is based upon the assumption that the models of Truelove & McKee (1999) are suitable for G266.2–1.2. Although Truelove & McKee (1999) only considered uniform ambient densities, it is possible to obtain a simple scaling factor between the age obtained using their model and the age expected if the ambient material has a mass density distribution  $\rho \propto r^{-s}$ . At early

times (i.e. those for which  $t < 0.5t_{\text{ch}}$ ), the effective value of  $m$  would be given by  $(n - 3)/(n - s)$ , not  $(n - 3)/n$  (Truelove & McKee 1999). As a result,  $m$ , and hence the age, is larger by a factor of  $n/(n - s)$ . Therefore, if the ambient material is from a steady wind (i.e.  $s = 2$ ) and if  $n \geq 6$ , then the age is underestimated by no more than a factor of 1.5.

The remnant was most likely produced by a core collapse supernova:<sup>16</sup> (1) There are reports of an X-ray emitting compact central object (Aschenbach 1998; Slane et al. 2001; Pavlov et al. 2001). (2) There is no evidence of thermal X-ray emission, which suggests that G266.2–1.2 is expanding into the rarefied environment of a stellar wind-blown bubble (Slane et al. 2001; Lee et al. 2013). (3) There is a molecular cloud (the Vela Molecular Ridge) and a group of massive stars (i.e. Vel OB1, Eggen 1982) with which the remnant may be associated. Yet, if G266.2–1.2 is the remnant of a Type Ia supernova, instead of a core collapse event, then Dwarkadas & Chevalier (1998) suggest the ejected material may have an exponential mass density distribution  $\rho_{\text{ej}} \propto e^{-v}t^{-3}$  instead of a power-law distribution  $\rho_{\text{ej}} \propto v^{-n}t^{-3}$ . Although Truelove & McKee (1999) did not consider models with exponential ejecta profiles, Dwarkadas & Chevalier (1998) note that Type Ia remnants have been modeled using a power law with  $n = 7$ . If the sample of plausible scenarios is limited to the subset with  $n = 7$  and with  $M_{\text{ej}} = 1.4M_{\odot}$ , then the 90% confidence level interval for the age is from 2.4 to 4.5 kyr with no scenario having an age less than 2.2 kyr or more than 6.1 kyr.

For these reasons, the age of G266.2–1.2 is expected to be between 2.4 and 5.1 kyr whether or not it was produced by a core collapse supernova. In no case is the remnant expected to be younger than 2.2 kyr, which contradicts most of the previous age estimates. These estimates are reviewed hereafter.

The first estimate published was that of Aschenbach (1998), who argues that G266.2–1.2 is less than or about 1.5 kyr old. This result is based upon the high temperature that is obtained when the *ROSAT* PSPC data are fitted with a thermal emission model. However, subsequent observations with the *ASCA* GIS (Tsunemi et al. 2000), which had better spectral resolution, reveal that the X-ray flux is dominated by synchrotron radiation and show no evidence of thermal emission (Slane et al. 2001).

Several age estimates are based upon evidence of emission associated with the decay of <sup>44</sup>Ti. Iyudin et al. (1998) report an emission line at 1.16 MeV in *COMPTEL* data and obtain an age of about 0.68 kyr. Chen & Gehrels (1999) and Aschenbach et al. (1999) expand upon this work and find ages between 0.6 and 1.1 kyr and less than 1.1 kyr, respectively. Tsunemi et al. (2000) report the detection of a  $4.1 \pm 0.2$  keV X-ray emission line from the northwestern rim with *ASCA*. They attribute this line to <sup>44</sup>Ca produced by the decay of <sup>44</sup>Ti. Based upon the 1.16 MeV line flux, they estimate an age between 0.6 and 1.0 kyr. Slane et al. (2001) reexamined the *ASCA* data. While they find a hint of a 4 keV line in the *SIS0* data for a region in the northwest, they find

---

<sup>16</sup>Iyudin et al. (2005) argue that G266.2–1.2 was produced by a sub-Chandrasekhar Type Ia supernova. However, this argument is based, in part, on the unlikely assumption that the remnant emits an observable flux of 1.16 MeV gamma rays associated with the decay of <sup>44</sup>Ti (Iyudin et al. 1998).

no such evidence in the SIS1 data for the same region. Iyudin et al. (2005) report a line feature at  $4.45 \pm 0.05$  keV in *XMM-Newton* spectra for the northwestern, western, and southern rims. Hiraga et al. (2009) find no evidence of a 4 keV emission line in *Suzaku* data. Their upper limits on the line flux are well below the line fluxes reported by Tsunemi et al. (2000), Iyudin et al. (2005), and Bamba et al. (2005). Their limits are also below the X-ray line flux inferred from the gamma-ray line flux of Iyudin et al. (1998). Furthermore, there is some concern about the statistical significance of the 1.16 MeV line in the *COMPTEL* data (Schönfelder et al. 2000) and there is no evidence of 67.9 and 78.4 keV lines in the *INTEGRAL* data (Renaud et al. 2006). Since the evidence of X-ray and gamma-ray emission lines associated with the decay of  $^{44}\text{Ti}$  is questionable, claims of their detections do not provide a compelling reason to doubt the age range inferred from the measurement of the expansion rate.

Following suggestions that G266.2–1.2 is young, Burgess & Zuber (2000) searched for evidence of a geophysical signature of the supernova that produced it. They report that South Pole ice core samples exhibit temporal spikes in the abundance of nitrate and that these spikes may be associated with historic supernovae. Their Figure 1 shows spikes that could be associated with the Kepler, Tycho, and AD 1181 supernovae. It also shows a spike that occurred in  $\text{AD } 1320 \pm 20$ . If this spike is associated with G266.2–1.2, then the age of the spike would be consistent with ages inferred from the reports of  $^{44}\text{Ti}$  line emission. However, they note that it is not clear that the ionizing radiation from supernovae significantly affect the terrestrial nitrate abundance. For example, there is no spike associated with Cas A. Unfortunately, the results presented in their figure do not go back far enough to determine whether or not there are spikes associated with the Crab and SN 1006 supernovae.

Obergaulinger et al. (2014) performed a hydrodynamic analysis assuming that G266.2–1.2 is expanding into an environment with several molecular clouds that have a variety of masses and densities. While they note that they cannot eliminate the possibility that the remnant is a few thousand years old, they favor an age of about 0.8 kyr. Unfortunately, it’s not clear that their assumptions are applicable to G266.2–1.2. For example, there’s no clear evidence that the remnant is expanding into a medium with a large density gradient. In their simulated images, the X-ray emission from the rim of the remnant is irregularly shaped and clumpy, unlike the observations, which show an outer edge that follows a nearly circular arc in the northwest (Figs. 1 and 2). Furthermore, the X-ray emission in their model is entirely thermal, whereas the X-ray emission from the remnant is dominated by nonthermal emission, at least above about 1 keV. In fact, the conditions of their model (i.e. a downstream shock-heated plasma with  $n = 1 \text{ cm}^{-3}$  and  $kT = 1 \text{ keV}$ ) are incompatible with the limits obtained from the *ROSAT* data. If  $kT = 1 \text{ keV}$ , then the downstream density cannot be larger than  $0.4 \text{ cm}^{-3}$ . For these reasons, the results of their analysis may not be accurate for G266.2–1.2.

Bamba et al. (2005) infer an age between 0.42 and 1.4 kyr using a novel technique. This technique is based upon a simple hydrodynamic model and upon a relationship between the age and the quantity  $\nu_{\text{roll}}/l^2$ , where  $\nu_{\text{roll}}$  and  $l$  are the roll-off frequency and downstream scale length

of X-ray synchrotron radiation, respectively. At present, there is too little data to evaluate its reliability.

Of the previously-published ages, 17.5 kyr (Telezhinsky 2009) is unique in that it is larger than the ages inferred from the *Chandra* data. Telezhinsky suggests that G266.2–1.2 entered the radiative phase 1.5 kyr ago. As a result, a significant fraction of the thermal energy of the shock-heated gas has been lost. Therefore, it’s possible to have a large ambient density ( $n_0 = 1.5 \text{ cm}^{-3}$ ) without the thermal X-ray emission being higher than observational constraints. The large density means that the TeV gamma-ray emission can be described primarily in terms of the photons produced by neutral-pion decay instead of inverse Compton scattering. However, it’s not clear that this model is consistent with the detection of thin, X-ray–synchrotron-dominated filaments. These filaments, which are thought to be associated with the forward shock, have synchrotron cut-off frequencies in excess of  $10^{17}$  Hz (Pannuti et al. 2010). Using Telezhinsky’s magnetic field strength of  $67 \mu\text{G}$ , the corresponding electron cut-off energy is greater than 10 TeV. Yet, if particle acceleration at the forward shock ended 1.5 kyr ago (Telezhinsky 2009), then electrons with energies in excess of 1 TeV would have lost their energy via synchrotron radiation. The synchrotron spectrum would have a cut-off frequency of about  $10^{15}$  Hz and would not be detectable at X-ray energies. Another concern is that the model may violate energy conservation. For example, the amount of energy transferred to the bulk kinetic motion and to the random thermal motion of the forward-shocked material (even if some of this energy has been lost via radiation) may be expressed as  $U_f \equiv U_{KE,f} + U_{kT,f} = 3\pi\rho_0 r_f^3 v_f^2 / 4 = 1.96 \times 10^{53} (n_0 / 1 \text{ cm}^{-3}) (\theta / 1^\circ)^3 (\dot{\theta} / 1 \text{ arcsec yr}^{-1})^2 (d / 1 \text{ kpc})^5$  ergs. Using Telezhinsky’s values of  $n_0$  ( $1.5 \text{ cm}^{-3}$ ) and  $d$  (0.6 kpc) and our values of  $\theta$  ( $0.86^\circ$ ) and  $\dot{\theta}$  ( $0.42 \text{ arcsec yr}^{-1}$ ), yields  $U_f = 2.57 \times 10^{51}$  ergs. Although this computation excludes all other forms of energy, the value of  $U_f$  is still much larger than Telezhinsky’s initial kinetic energy of  $2 \times 10^{50}$  ergs.

In summary, a wide range of ages have been inferred for G266.2–1.2 using a variety of different evidence. Of these reports, we argue that the most reliable are those based upon the measurement of the expansion rate of the remnant. The biggest concern with this technique is that the expansion rate in the northwest may not be representative of the remnant as a whole. If the *Chandra* results are accurate and representative, then G266.2–1.2 is between 2.4 and 5.1 kyr old.

### 3.2. Distance

The measured expansion rate, even when coupled with the hydrodynamic simulations, does not provide a significant constraint on the distance. For example, Figure 7 shows that the range from 0.7 to 3.2 kpc encompasses 90% of the 57.4 million scenarios that satisfy the plausibility criteria described in §3.1. The full range of distances for these scenarios is from 0.3 to 4.5 kpc. Hereafter, we review other inferences about the distance.

If, as expected, the remnant was produced by a core collapse supernova, then it is likely that it

is part of the Vela Molecular Ridge. This material is concentrated into two groups (Murphy & May 1991), one at a distance of  $0.7 \pm 0.2$  kpc (Liseau et al. 1992) and the other at a distance of about 2 kpc. In particular, the progenitor of G266.2–1.2 may have been a member of either the Vel OB1 or Vel OB2<sup>17</sup> associations, which are at distances of about 0.8 and 1.8 kpc, respectively (Eggen 1982). Duncan & Green (2000) report that a distance of 1–2 kpc, instead of a distance much less than 1 kpc, yields a diameter that is more compatible with the diameters of remnants that have similar radio surface brightnesses (see their Fig. 6).

Reynoso et al. (2006) use the column density  $n_{\text{H}}$  toward the central compact object CXOU J085201.4–461753, as measured by Becker & Aschenbach (2002), to infer a distance of  $2.4 \pm 0.4$  kpc. However, Acero et al. (2013) show that most of the column density along this line of sight (and toward the remnant) is associated with the Vela Molecular Ridge. Therefore, the compact object (and G266.2–1.2) can be no further than 0.9 kpc. This limit is consistent with the results of Kim et al. (2012), who suggest that the remnant may be a source of far-ultraviolet emission, in which case it is closer than 1 kpc.

Since the values of  $n_{\text{H}}$  associated with G266.2–1.2 are significantly larger than the values associated the Vela supernova remnant (Slane et al. 2001), the remnant must lie beyond Vela ( $d_{\text{Vela}} = 0.29 \pm 0.02$  kpc, Dodson et al. 2003). A more restrictive lower limit can be obtained from the properties of the X-ray synchrotron emission in the northwest. Since the synchrotron cut-off frequency exceeds  $10^{17}$  Hz (Pannuti et al. 2010), the shock speed must be larger than about  $1000 \text{ km s}^{-1}$  (Allen et al. 2008), which implies that the distance  $d = v_{\text{f}}/\dot{\theta} > 0.5$  kpc.

Conversely, Aschenbach (2013) argues that the remnant is closer, perhaps much closer, than 0.5 kpc. This argument hinges upon the assumption that the gamma-ray emission is dominated by neutral-pion decay.<sup>18</sup> Yet, Berezhko et al. (2009) could not make such a model work if the remnant is nearby. Furthermore, if the *Fermi* spectrum of Tanaka et al. (2011) includes emission from both G266.2–1.2 and PSR J0855–4644, particularly at the lower end of their spectrum, then an inverse Compton scattering model may provide a better description of the gamma-ray emission from G266.2–1.2 (e.g. Katsuda et al. 2008a; Lee et al. 2013).

Early estimates of the distance, based upon evidence of line emission associated with the decay of <sup>44</sup>Ti, also suggest the source is nearby [e.g.  $d = 0.2$  kpc, (Iyudin et al. 1998);  $d = 0.1$ – $0.3$  kpc, (Chen & Gehrels 1999); and  $d < 0.5$  kpc, (Aschenbach et al. 1999)]. However, as described in §3.1, this evidence is questionable.

In summary, the preponderance of the distance results suggests that G266.2–1.2 is between

---

<sup>17</sup>The Vel OB2 association of Eggen (1982) should not be confused with an entirely different association referred to as Vela OB2 by de Zeeuw et al. (1999).

<sup>18</sup>Although we use the same energy constraints as Aschenbach (2013), we assume that the TeV gamma rays are dominated by inverse Compton scattering instead of neutral-pion decay. In this case, it is possible for the remnant to be considerably more distant than 0.5 kpc.

about 0.5 and 1 kpc from Earth. Hereafter, we assume the remnant is at a distance of  $0.7 \pm 0.2$  kpc. Note that this assumption does not significantly affect the constraints on the age. Table 4 lists sample hydrodynamic properties for G266.2–1.2, assuming it is at a distance of either 0.5, 0.7, or 0.9 kpc. These properties include the initial kinetic energy,  $E_0$ , the mass,  $M_{\text{ej}}$ , and the power-law index,  $n$ , of the ejected material, the ambient density,  $n_0$ , the age,  $t$ , the radius,  $r_f$ , and speed,  $v_f$ , of the forward shock, the expansion parameter,  $m$ , the mass of the material swept up by the forward shock,  $M_s$ , and the amount of kinetic energy that has been transferred to this material,  $U_{\text{KE},f}$ . The values in the Table, which are based upon the results of the hydrodynamic study described in §3.1, are only meant to be representative. The values for each property can vary substantially from the listed values for individual scenarios. The value of  $n$  was arbitrarily chosen to be nine. As a result, the value of  $m = 2/3$ . The value of  $E_0$  was arbitrarily chosen to be  $10^{51}$  ergs, except for the case with  $d = 0.5$  kpc. At the closer distance, which is at the low end of the distribution in Figure 7, none of the scenarios with  $E_0 = 10^{51}$  ergs (or with  $E_0 > 10^{51}$  ergs) satisfied all of the plausibility criteria.

#### 4. Conclusions

We reprocessed and analyzed our 2003 and 2008 *Chandra* ACIS data for the supernova remnant G266.2–1.2 to search for evidence of expansion (e.g. Katsuda et al. 2008a). Two objects satisfy our criteria for potential registration sources. Instrumental simulations reveal no evidence of a significant registration error. For this reason, and because the expansion results are insensitive to small registration errors (Fig. 5), no registration adjustments were applied. The data for two adjacent annular wedges along a relatively bright and narrow portion of the northwestern rim indicate that it has experienced a radial displacement of about  $2.40 \pm 0.56$  arcsec over a period of 5.652 yr. The corresponding expansion rate ( $0.42 \pm 0.10$  arcsec yr<sup>-1</sup> or  $13.6 \pm 4.2\%$  kyr<sup>-1</sup>) is about half of the rate reported for an analysis of *XMM-Newton* data from a similar time interval and a similar region (Katsuda et al. 2008a). Since the regions used are not identical, one possible explanation for this difference is an azimuthal variation in the expansion rate. Additional observations would provide a more precise measure of the mean expansion rate and enable a search for azimuthal variations.

To constrain the age, a hydrodynamic analysis was performed using the models of Truelove & McKee (1999). Billions of scenarios were considered using broad ranges of initial kinetic energies, ejecta masses, ejecta mass density distributions, ambient densities, and evolutionary states to try to encompass all possible sets of hydrodynamic properties. Of these scenarios, 57.4 million are considered plausible because their properties are consistent with the *Chandra* expansion rate (assuming it is representative of the remnant as a whole), an inferred lower limit on the forward shock speed (1000 km s<sup>-1</sup>), an inferred upper limit on the thermal X-ray emission, and an energy constraint. Ninety percent of the plausible scenarios have ages in the range from 2.4 to 5.1 kyr. The age of G266.2–1.2 is most likely in this range whether or not it was produced by a Type Ia or Type II event. If the remnant is expanding into the material shed by a steady stellar wind instead of a

uniform ambient medium, then it could be older by a factor of up to 1.5. In no case is the remnant expected to be younger than 2.2 kyr. Since the measurements of the expansion rate seem to provide a more reliable means of determining the age than other techniques that have been used (see §3.1), G266.2–1.2 is most likely too old to be associated with emission from the decay of  $^{44}\text{Ti}$  or with features in the abundance of nitrate in South Pole ice core samples.

We set a lower limit on the distance of 0.5 kpc. This limit is based upon the *Chandra* expansion rate and the requirement that the shock speed be greater than or equal to  $1000 \text{ km s}^{-1}$ . (The detection of X-ray synchrotron emission is not expected for lower shock speeds.) An analysis of previously-published distance estimates and constraints suggests that the remnant is no more than 1.0 kpc from Earth. Therefore the distance of G266.2–1.2 is consistent with the distance of the closer of two groups of material in the Vela Molecular Ridge (i.e.  $0.7 \pm 0.2$  kpc, Liseau et al. 1992). This distance is also consistent with the progenitor having been a member of the Vel OB1 association (Eggen 1982) and with our estimates of the age range. Note that constraining the distance does not significantly affect the estimate of the age.

We thank the anonymous referee, whose comments helped improve the manuscript. G.E.A. is supported by contract SV3-73016 between MIT and the Smithsonian Astrophysical Observatory. The Smithsonian Astrophysical Observatory is operated on behalf of NASA under contract NAS8-03060. This research has made use of data products from the Chandra Data Archive, the Two Micron All Sky Survey, and the USNO-B1.0 catalog. The analyses described herein were performed using the software package CIAO, provided by the Chandra X-ray Center, the software package ISIS (Houck & Denicola 2000), the scripting language S-Lang, and models of the XSPEC spectral-fitting package.

*Facilities:* CXO (ACIS).

## REFERENCES

- Acerro, F., Gallant, Y., Ballet, J., Renaud, M., & Terrier, R. 2013, *A&A*, 551, A7
- Aharonian, F., Akhperjanian, A. G., Bazer-Bachi, A. R., et al. 2005, *A&A*, 437, L7
- Aharonian, F., Akhperjanian, A. G., Bazer-Bachi, A. R., et al. 2007, *ApJ*, 661, 236
- Allen, G. E., Houck, J. C., & Sturmer, S. J. 2008, *ApJ*, 683, 773
- Allen, G., DeLaney, T., Filipović, et al. 2011, in *Extreme and Variable High Energy Sky (Extremesky 2011)*, 40, <http://adsabs.harvard.edu/abs/2011evhe.confE..40A>
- Aschenbach, B. Iyudin, A. F., & Schönfelder, V., 1999, *A&A*, 350, 997
- Aschenbach, B. 1998, *Nature*, 396, 141



- Aschenbach, B. 2013, *Acta Polytechnica*, 53, 617
- Bamba, A., Yamazaki, R., & Hiraga, J. S. 2005, *ApJ*, 632, 294
- Bamba, A., Yamazaki, R., Yoshida, T., Terasawa, T., & Koyama, K. 2005, *ApJ*, 621, 793
- Becker, W., & Aschenbach, B. 2002, in *Neutron Stars, Pulsars, and Supernova Remnants*, ed. W. Becker, H. Lesch, & J. Trümper, 64
- Becker, W., Hui, C. Y., Aschenbach, B., & Iyudin, A. 2006, arXiv:astro-ph/0607081
- Berezhko, E. G., Pühlhofer, G., & Völk, H. J. 2009, *A&A*, 505, 641
- Burgess, C. P., & Zuber, K. 2000, *Astropart. Phys.*, 14, 1
- Bock, D. C.-J., Turtle, A. J., & Green, A. J. 1998, *ApJ*, 116, 1886
- Castor, J., McCray, R., & Weaver, R. 1975, *ApJ*, 200, L107
- Chen, W., & Gehrels, N. 1999, *ApJ*, 514, L103
- Combi, J. A., Romero, G. E., & Bengaglia, P. 1999, *ApJ*, 519, L177
- de Zeeuw, P. T., Hoogerwerf, R., de Bruijne, J. H. J., Brown, A. G. A., & Blaauw, A. 1999, *AJ*, 117, 354
- DeLaney, T., & Rudnick, L. 2003, *ApJ*, 589, 818
- Dodson, R., Legge, D., Reynolds, J. E., & McCulloch, P. M. 2003, *ApJ*, 596, 1137
- Dubner, G. M., Green, A. J., Goss, W. M., Bock, D. C.-J., & Giacani, E. 1998, *AJ*, 116, 813
- Duncan, A. R., & Green, D. A. 2000, *A&A*, 364, 732
- Dwarkadas, V. V., & Chevalier, R. A. 1998, *ApJ*, 497, 807
- Eggen, O. J. 1982, *ApJS*, 50, 199
- Enomoto, R., Watanabe, S., & Tanimori, T., et al. 2006, *ApJ*, 652, 1268
- Filipović, M. D., Jones, P. A., & Aschenbach, B. 2001, in *AIP Conf. Ser. 565, Young Supernova Remnants*, ed. S. S. Holt & U. Hwang, 267
- Hiraga, J. S., Kobayashi, Y., Tamagawa, T., et al. 2009, *PASJ*, 61, 275
- Houck, J. C., & Denicola, L. A. 2000, in *ASP Conf. Ser. 216, Astronomical Data Analysis Software and Systems IX*, ed. N. Manset, C. Veillet, & D. Crabtree, 591
- Iyudin, A. F., Aschenbach, B., Becker, W., Dennerl, K., & Haberl, F. 2005, *A&A*, 429, 225

- Iyudin, A. F., Schönfelder, V., Bennett, K., et al. 1998, *Nature*, 396, 142
- Kargaltsev, O., Pavlov, G. G., Sanwal, D., & Garmire, G. P. 2002, *ApJ*, 580, 1060
- Katagiri, H., Enomoto, R., Ksenofontov, L. T., et al. 2005, *ApJ*, 619, L163
- Katsuda, S., Petre, R., Long, K. S., et al. 2009, *ApJ*, 692, L105
- Katsuda, S., & Tsunemi, H. 2005, *PASJ*, 57, 621
- Katsuda, S., & Tsunemi, H. 2006, *ApJ*, 642, 917
- Katsuda, S., Tsunemi, H., & Mori, K. 2008a, *ApJ*, 678, L35
- Katsuda, S., Tsunemi, H., Uchida, H., & Kimura, M. 2008b, *ApJ*, 689, 225
- Kim, I.-J., Seon, K.-I., Min, K.-W., Han, W., & Edelstein, J. 2012, *ApJ*, 761, 135
- Kramer, M., Bell, J. F., Manchester, R. N., et al. 2003, *MNRAS*, 342, 1299
- Lande, J., Ackermann, M., Allafort, A., et al. 2012, *ApJ*, 756, 5
- Lee, S.-H., Slane, P. O., Ellison, D. C., Nagataki, S., & Patnaude, D. J. 2013, *ApJ*, 767, 20
- Liseau, R., Lorenzetti, D., Nisini, B., Spinoglio, L., & Moneti, A. 1992, *A&A*, 265, 577
- Manchester, R. N., Hobbs, G. B., Teoh, A., & Hobbs, M. 2005, *AJ*, 129, 1993
- Mereghetti, S. 2001, *ApJ*, 548, L213
- Mignani, R. P., de Luca, A., & Pellizzoni, A. 2009, *A&A*, 508, 779
- Mignani, R. P., de Luca, A., Zaggia, S., et al. 2007, *A&A*, 473, 883
- Milne, D. K. 1968, *Aust. J. Phys.*, 21, 201
- Miyata, E., Tsunemi, H., Aschenbach, B., & Mori, K. 2001, *ApJ*, 559, L45
- Monet, D. G., Levine, S. E., Canzian, B., et al. 2003, *AJ*, 125, 984
- Murphy, D. C., & May, J. 1991, *A&A*, 247, 202
- Nichols, J. S., & Slavin, J. D. 2004, *ApJ*, 610, 285
- Nishikida, K., Edelstein, J., Korpela, E. J., et al. 2006, *ApJ*, 644, L171
- Obergaulinger, M., Iyudin, A. F., Müller, E., & Smoot, G. F. 2014, *MNRAS*, 437, 976
- Ogasawara, T., Yoshida, T., Yanagita, S., & Kifune, T. 2007, *Ap&SS*, 309, 401
- Pannuti, T. G., Allen, G. E., Filipović, M. D., et al. 2010, *ApJ*, 721, 1492

- Pavlov, G. G., Sanwal, D., Kiziltan, B., & Garmire, G. P. 2001, *ApJ*, 559, L131
- Pellizzoni, A., Mereghetti, S., & De Luca, A. 2002, *A&A*, 393, L65
- Plucinsky, P. P., Smith, R. K., Edgar, R. J., et al. 2002, in *ASP Conf. Ser.* 271, ed. P. O. Slane & B. M. Gaensler, 407
- Redman, M. P., & Meaburn, J. 2005, *MNRAS*, 356, 969
- Renaud, M., Vink, J., Decourchelle, A., et al. 2006, *New A Rev.*, 50, 540
- Reynoso, E. M., Dubner, G., Giacani, E., Johnston, S., & Green, A. J. 2006, *A&A*, 449, 243
- Schönfelder, V., Bloemen, H., Collmar, W., et al. 2000, in *AIP Conf. Ser.* 510, ed. M. L. McConnell & J. M. Ryan, 54
- Slane, P., Hughes, J. P., Edgar, R. J., et al. 2001, *ApJ*, 548, 814
- Stupar, M., Filipović, M. D., Jones, P. A., & Parker, Q. A. 2005, *Adv. Space Res.*, 35, 1047
- Tanaka, T., Allafort, A., Ballet, J., et al. 2011, *ApJ*, 740, L51
- Testori, J. C., Arnal, E. M., Morras, R., et al. 2006, *A&A*, 458, 163
- Telezhinsky, I. 2009, *Astropart. Phys.*, 31, 431
- Truelove, J. K., & McKee, C. F. 1999, *ApJS*, 120, 299
- Tsunemi, H., Miyata, E., Aschenbach, B., Hiraga, J., & Akutsu, D. 2000, *PASJ*, 52, 887
- Wang, C.-Y., & Chevalier, R. A. 2002, *ApJ*, 574, 155

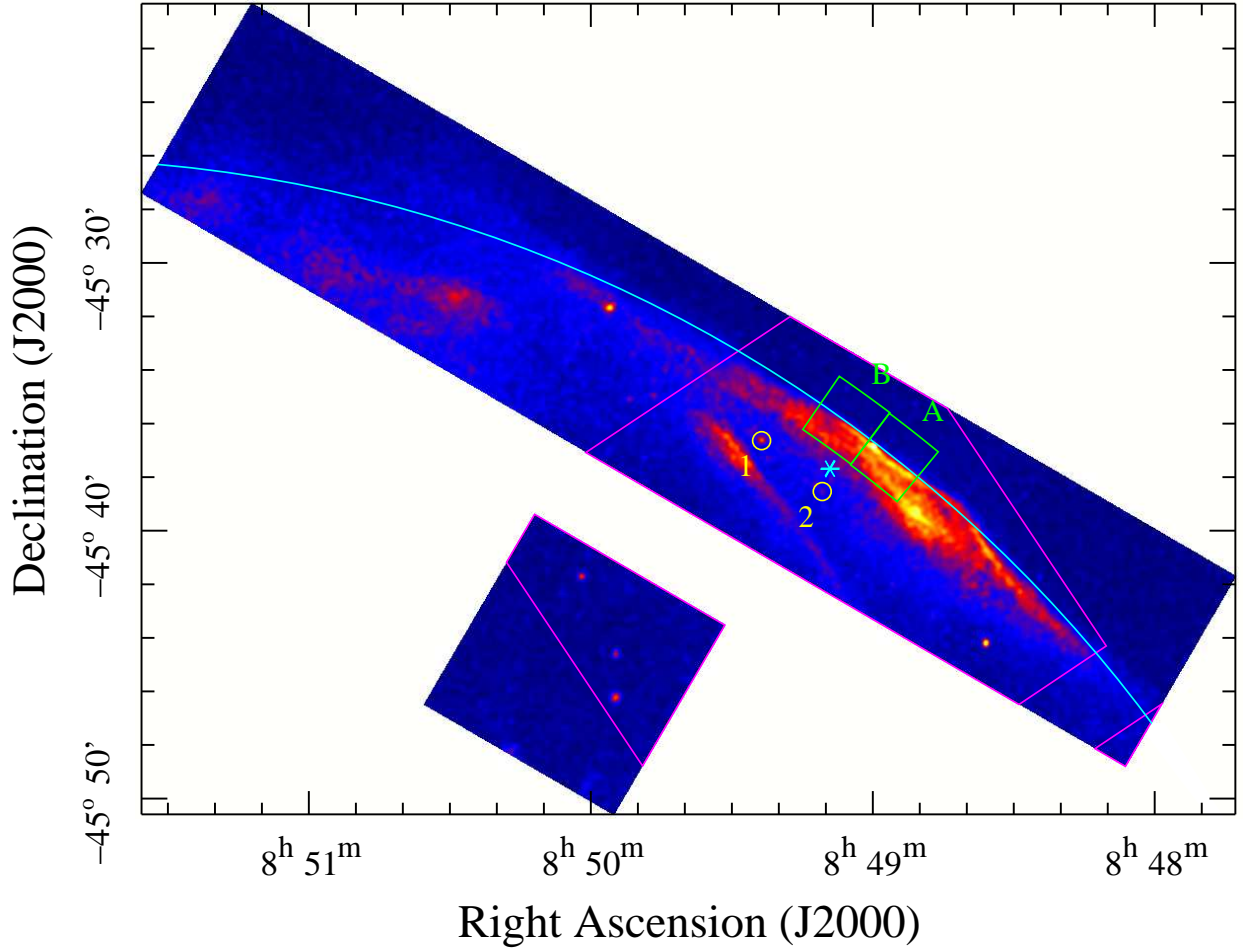


Fig. 1.— A 1–5 keV image of the northwestern rim of G266.2–1.2 from the 2003 *Chandra* observation. The cyan asterisk is the location of the aim point. The image has been adjusted to compensate for instrumental effects, to the extent possible, and smoothed using a two-dimensional Gaussian function with  $\sigma_X = \sigma_Y = 10$  pixels = 4.92 arcsec. The color is a linear function of the flux and varies from about  $1 \times 10^{-9}$  or less (dark blue) to  $1.4 \times 10^{-8}$  or more (white) in units of photons  $\text{cm}^{-2} \text{s}^{-1} \text{pixel}^{-1}$ . The magenta lines mark the boundary of the region that was observed in both 2003 and 2008. The yellow circles encompass registration sources 1 and 2. The green annular wedges mark the boundaries of regions A and B, which were used to measure the rate of expansion. The cyan arc is a segment of a circle that has a radius of  $0.8642^\circ$  and that is centered on the location of CXOU J085201.4–461753 (Pavlov et al. 2001).

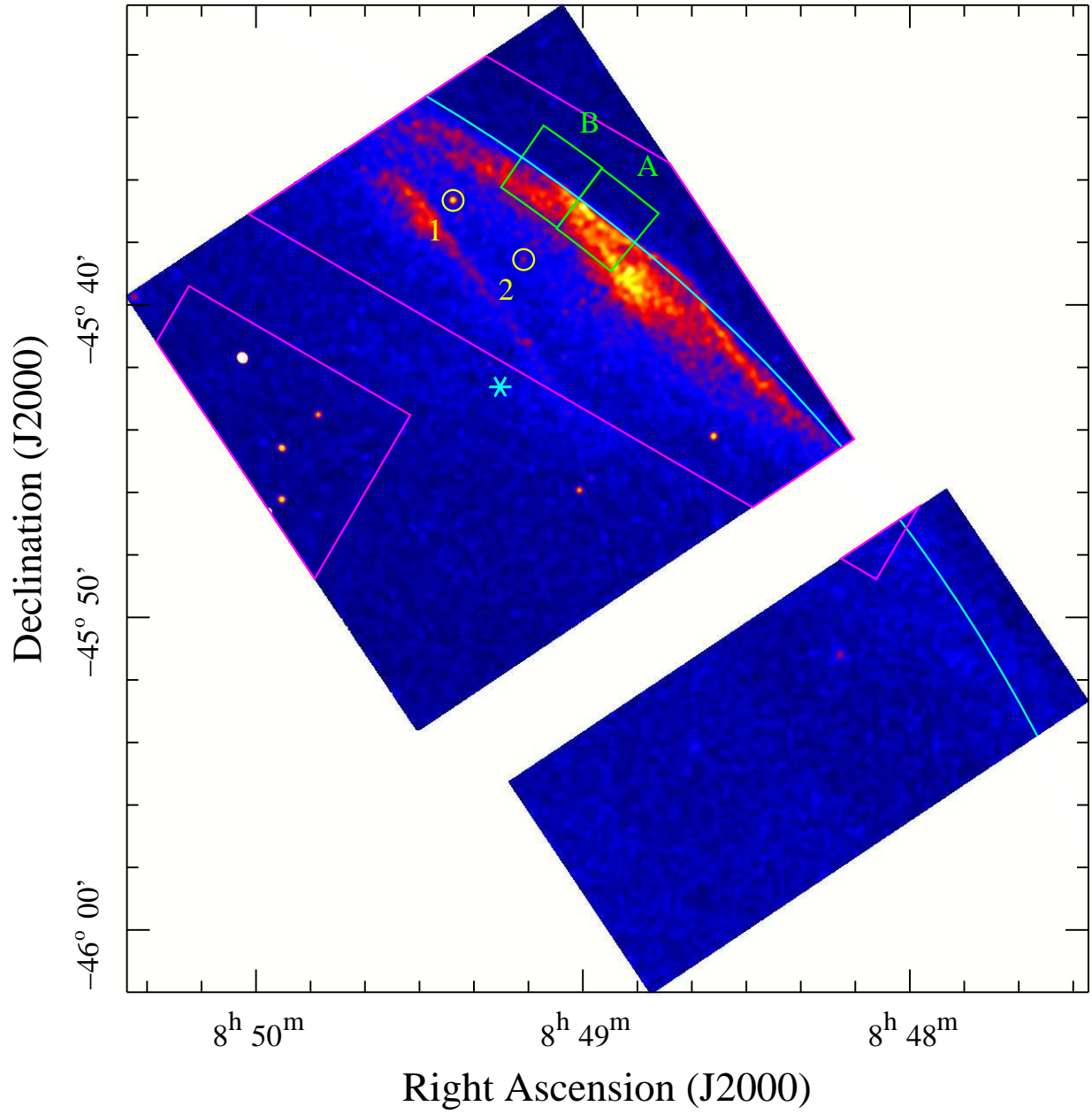


Fig. 2.— A 1–5 keV image of the northwestern rim of G266.2–1.2 from the 2008 *Chandra* observation. Refer to the caption of Figure 1 for more details.

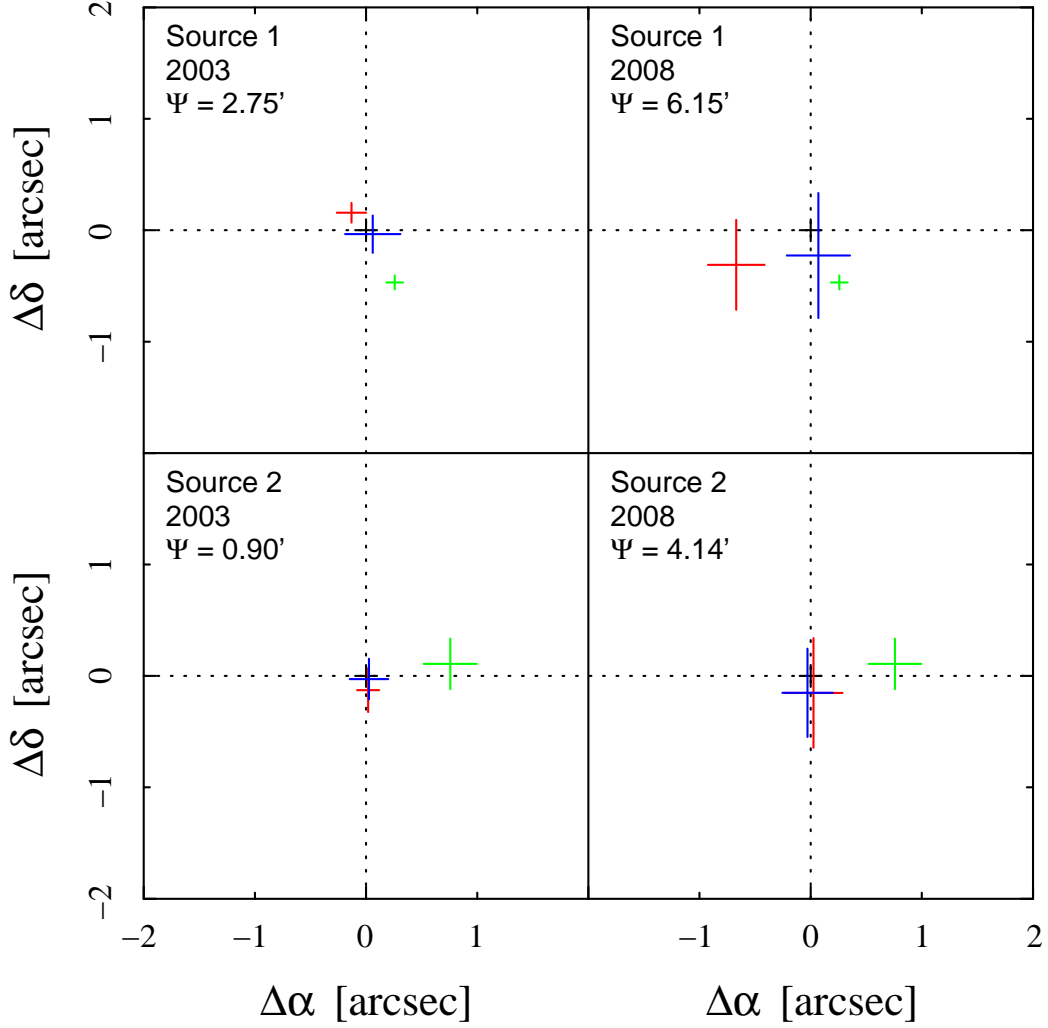


Fig. 3.— A comparison of the actual *Chandra* (red), expected *Chandra* (blue, see text), *2MASS* (black), and USNO-B1.0 (green) locations of the two registration sources. Here,  $\Delta\alpha = \alpha_{\text{obs}} - \alpha_{2MASS}$  and  $\Delta\delta = \delta_{\text{obs}} - \delta_{2MASS}$ , where the subscript obs is either *Chandra* or USNO-B1.0. The horizontal and vertical error bars denote the 90% confidence level intervals. The top and bottom panels are for source 1 and source 2, respectively. The left and right panels are for the 2003 and 2008 *Chandra* observations, respectively. The *2MASS* and USNO-B1.0 locations do not change from the left side to the right side. The angular separation between the registration source and the optical axis of *Chandra* is specified by  $\Psi$  in arcminutes.

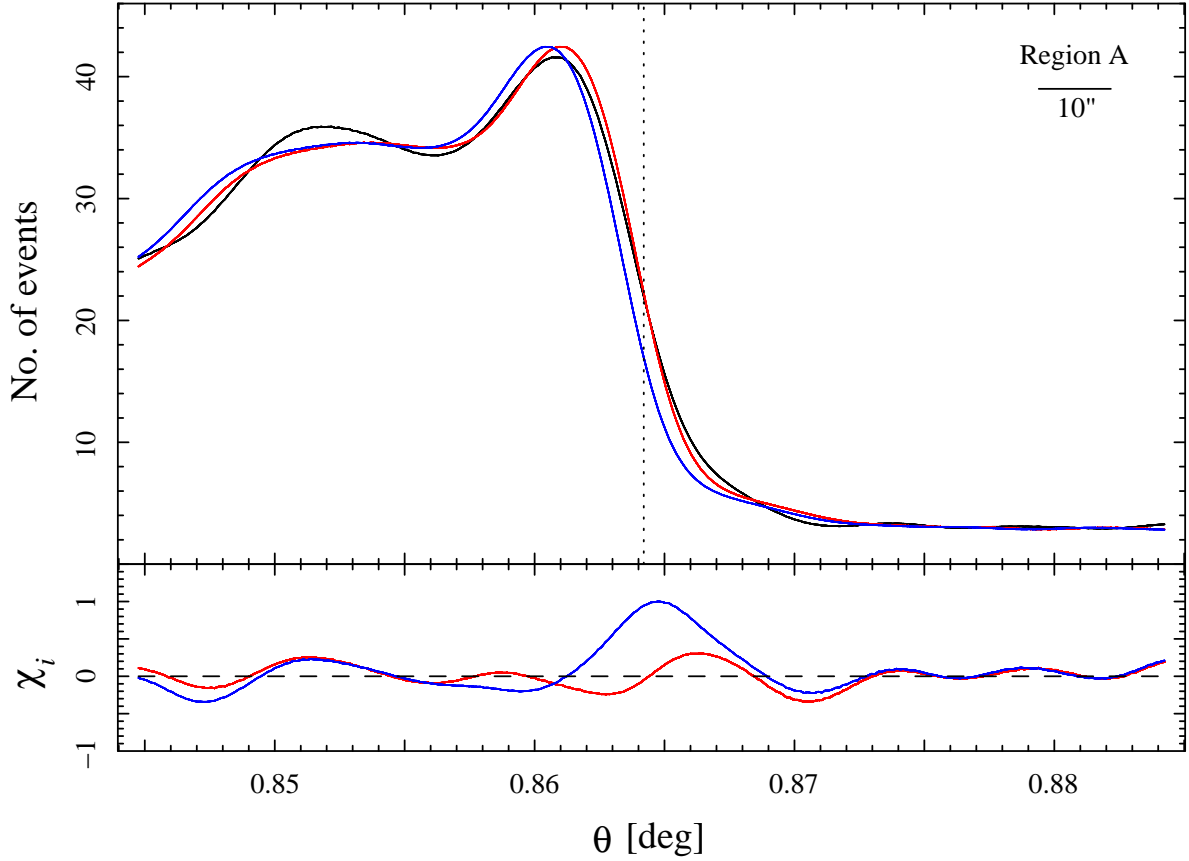


Fig. 4.— *Top panel:* Radial profiles for region A (see Figures 1 and 2). The black curve is the number of events in each radial bin from the 2008 dataset. Here, the bins are 1 pixel (0.492 arcsec) wide. The dotted vertical line at  $\theta = 0.8642^\circ$  is the radius at which the number of events in 2008 is halfway between the peak of the black curve and the nominal number of background events at the right side of the profile. The blue curve is the model before it has been radially shifted (i.e.  $M$  from eqn. 2 with  $j = 0$ ). A comparison of the blue and black curves shows that the change in the location of the forward shock from 2003 to 2008 is evident. The red curve is identical to the blue curve, except that it has been shifted to the right by 2.0 arcsec (Table 3). For comparison, the line segment in the upper, right-hand corner is 10 arcsec in length. *Bottom panel:* The differences between the black profile and the blue and red profiles divided by the  $1\text{-}\sigma$  statistical uncertainties (see eqn. 3).

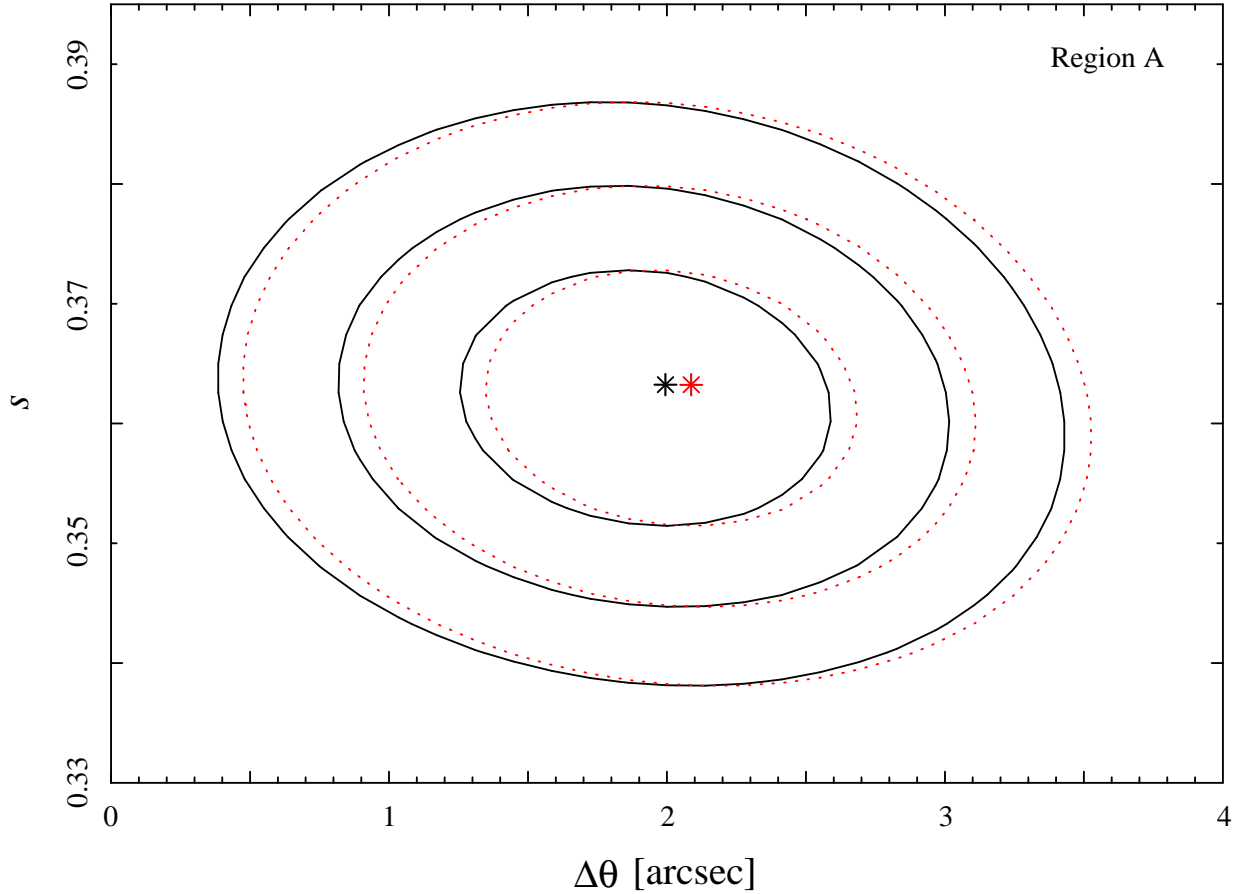


Fig. 5.— The 1-, 2-, and 3- $\sigma$  confidence contours for region A (see Figures 1 and 2) in the parameter space defined by the radial expansion  $\Delta\theta$  and the scaling factor  $s$ . The solid black and dotted red contours are the results obtained before and after, respectively, the mean  $\Delta\alpha$  and  $\Delta\delta$  registration adjustments (see sec. 2) are included. The stars indicate the best-fit values of  $\Delta\theta$  and  $s$ . The evidence of expansion in region A (i.e. the evidence that  $\Delta\theta > 0$ ) is significant at nearly the 4- $\sigma$  confidence level.



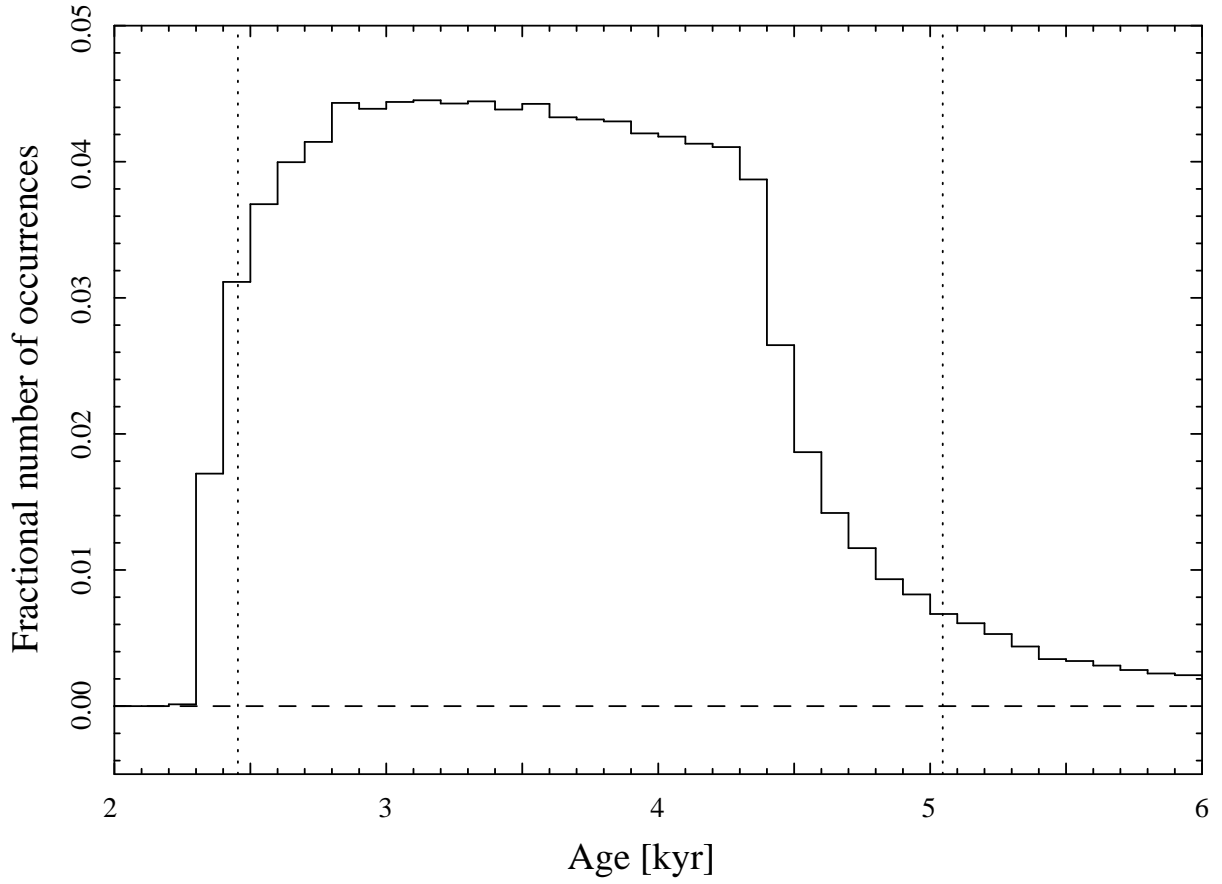


Fig. 6.— The distribution of the ages of the 57.4 million plausible hydrodynamic scenarios described in §3.1. If the lowest 5% and highest 5% of the distribution are ignored, then the plausible ages lie between about 2.4 and 5.1 kyr (i.e. between the dotted vertical lines).

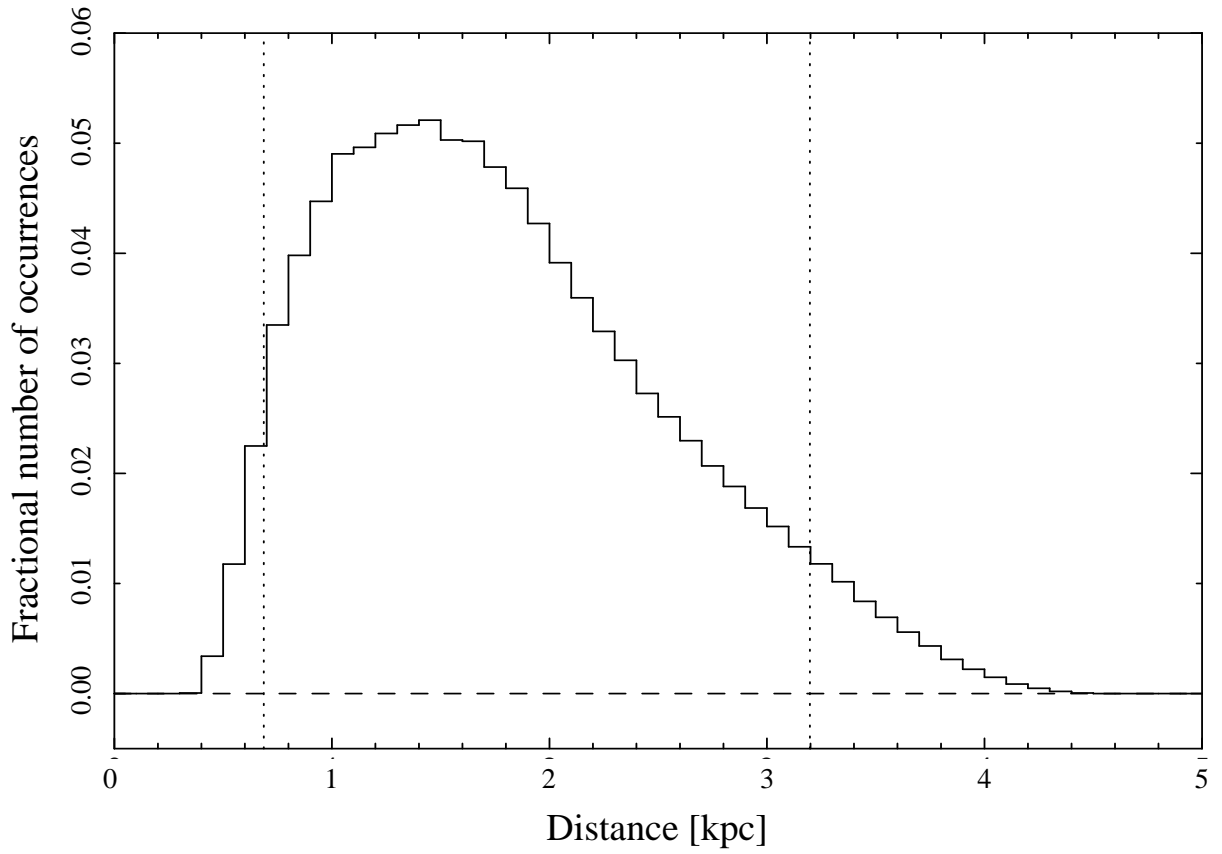


Fig. 7.— The distribution of the distances of the 57.4 million plausible hydrodynamic scenarios described in §3.1. If the lowest 5% and highest 5% of the distribution are ignored, then the plausible distances lie between about 0.7 and 3.2 kpc (i.e. between the dotted vertical lines).

Table 1. *Chandra* observations of the northwestern rim

	2003	2008
Observation IDs	3846, 4414	9123
Start date	2003 Jan 5	2008 Aug 31
End date	2003 Jan 7	2008 Sep 1
Duration [ks]	74	40
Pointing location:		
RA [J2000]	8 <sup>h</sup> 49 <sup>m</sup> 9.40 <sup>s</sup>	8 <sup>h</sup> 49 <sup>m</sup> 15.34 <sup>s</sup>
Dec [J2000]	-45° 37' 42.4''	-45° 42' 37.7''
ACIS detectors used <sup>a</sup>	I2, S0, S1, S2, S3, S4	I0, I1, I2, I3, S2, S3
Maximum effective area <sup>b</sup> [cm <sup>2</sup> ]	700 @ 1.5 keV	575 @ 1.5 keV
Effective energy band <sup>c</sup> [keV]	0.4–7.5	0.6–7.8
Fractional energy resolution <sup>d</sup> [FWHM/ <i>E</i> ]:		
At 1 keV	0.10	0.13
At 5 keV	0.03	0.05

<sup>a</sup>Each 1024 pixel × 1024 pixel ACIS CCD has a field of view of 8.4 arcmin × 8.4 arcmin.

<sup>b</sup>The effective area is a function of energy and position. The values reported here are the largest values at the locations of the aim points. The maximum effective area declines away from these locations.

<sup>c</sup>Here, the effective energy band is the range over which the effective area at the aim point is greater than or equal to 10% of the maximum effective area.

<sup>d</sup>The fractional energy resolution is a function of energy and position. The values reported here are the values at the locations of the aim points.

Table 2. Registration sources

	Source 1			Source 2		
	ID	$\alpha^a$ [h m s]	$\delta^a$ [ $^{\circ}$ ' '' ]	ID	$\alpha^a$ [h m s]	$\delta^a$ [ $^{\circ}$ ' '' ]
<i>Chandra</i> 2003	1	08 49 23.935(13)	-45 36 39.59(9)	2	08 49 11.041(19)	-45 38 33.51(20)
<i>Chandra</i> 2008	1	08 49 23.883(24)	-45 36 40.06(40)	2	08 49 11.041(47)	-45 38 33.53(49)
2MASS <sup>b</sup>	08492394-4536397	08 49 23.947(16)	-45 36 39.75(10)	08491103-4538333	08 49 11.039(16)	-45 38 33.38(10)
USNO-B1.0 <sup>c</sup>	0443-0146834	08 49 23.971(7)	-45 36 40.22(6)	0443-0146664	08 49 11.111(23)	-45 38 33.27(23)

<sup>a</sup>The coordinates are in the J2000 epoch. The numbers in parentheses are the 90% confidence level uncertainties in units of  $10^{-3}$  seconds of Right Ascension or  $10^{-2}$  arcseconds of Declination.

<sup>b</sup>This information is from the 2MASS All-Sky Point Source catalog.<sup>9</sup>

<sup>c</sup>This information is from the USNO-B1.0 catalog.<sup>10</sup>

Table 3. Expansion results

Quantity <sup>a</sup>	Region A	Region B
Region boundaries:		
$\theta$ [deg]	0.8442–0.8842	0.8447–0.8847
$\phi$ [deg]	320.0–322.5	322.5–325.0
Model parameters:		
$\Delta\theta$ [arcsec]	$1.98 \pm 0.72$	$3.03 \pm 0.89$
$s$	$0.363 \pm 0.011$	$0.324 \pm 0.012$
$\Sigma_{B,2003}$ [events arcsec <sup>-2</sup> ]	$0.138 \pm 0.003^b$	$0.127 \pm 0.003^b$
$\Sigma_{B,2008}$ [events arcsec <sup>-2</sup> ]	$0.046 \pm 0.002^b$	$0.042 \pm 0.002^b$
Expansion:		
$\Delta t$ [yr]	5.652	5.652
$\dot{\theta} = \Delta\theta/\Delta t$ [arcsec yr <sup>-1</sup> ]	$0.35 \pm 0.13$	$0.54 \pm 0.16$
$\theta$ [deg]	$0.86 \pm 0.17^c$	$0.86 \pm 0.17^c$
$\dot{\theta}/\theta$ [kyr <sup>-1</sup> ]	$0.113 \pm 0.047$	$0.172 \pm 0.061$

<sup>a</sup>The statistical uncertainties are listed at the 90% confidence level.

<sup>b</sup>These values are based upon the sizes of and numbers of events in the source free portions of the regions.

<sup>c</sup>A 20% uncertainty in the shock radius is assumed because the location at which the progenitor exploded is unknown.

Table 4. Sample hydrodynamic properties

Property	Assumed distance		
	0.5 kpc	0.7 kpc	0.9 kpc
$E_0$ [ $10^{51}$ ergs]	0.5	1.0	1.0
$M_{\text{ej}}$ [ $M_{\odot}$ ]	50	40	28
$n$	9	9	9
$n_0$ [ $\text{cm}^{-3}$ ]	0.022	0.022	0.018
$t$ [kyr]	3.9	4.2	5.2
$r_f$ [pc]	8	11	14
$v_f$ [ $10^3$ km s $^{-1}$ ]	1.3	1.7	1.7
$m$	0.67	0.67	0.67
$M_s$ [ $M_{\odot}$ ]	1.4	3.9	6.6
$U_{\text{KE},f}$ [ $10^{50}$ ergs]	0.23	0.60	1.1